Available online at www.sciencedirect.com
ScienceDirect
Trans. Nonferrous Met. Soc. China 33(2023) 1522−1539
Transactions of Nonferrous Metals Society of China
www.tnmsc.cn

Influence of thermal diffusion treatment on microstructure evolution and corrosion behavior of hot-dipped Al coated Fe−Cr−Si−B cast steel

Xian-man ZHANG[1], Zai-yu CHEN[1], Xing-tao LI[1],
Kun-peng JI[1], Hong-feng LUO[1], Geng-ping WAN[2], Shao-feng YANG[3]

1. Mechanical and Electrical Engineering College, Hainan University, Haikou 570228, China;
2. Analytical & Testing Center, Hainan University, Haikou 570228, China;
3. School of Materials Science and Engineering, Nanjing Institute of Technology, Nanjing 211167, China

Received 7 December 2021; accepted 8 July 2022

Abstract: The influence of thermal diffusion treatment on the microstructure and corrosion behavior of hot-dipped Al coated Fe−Cr−Si−B cast steel in a 5 wt.% NaCl solution was studied. The results showed that the product obtained from the interfacial reaction between the Fe matrix in Fe−Cr−Si−B cast steel and molten Al was $FeAl_3$ with a columnar crystal structure. Periodic layered structures at the $(Cr, Fe)_2B$/Al interface were formed during the subsequent thermal diffusion treatment but not hot dip aluminizing. The corrosion behavior of the residual Al layer predominated that of the hot dip aluminizing and thermal diffusion treatment coatings over a short duration till the Al topcoat was consumed completely. Localized corrosion caused by Cl^- preferentially began from the block-like B−Al−Cr phase/$FeAl_3$ interface and propagated along periodic layered structures. The Si particles acted as a cathode and promoted the corrosion of the coating. The steel substrate retained its cathodic protection until the Fe−Al intermetallic compounds layer was corroded completely. Additionally, the corrosion in the NaCl solution at an elevated temperature was greatly accelerated.
Key words: hot dip aluminizing; thermal diffusion treatment; periodic layered structure; corrosion behavior; cathodic protection

1 Introduction

Corrosion of metals is a naturally occurring and unwanted phenomenon and has resulted in the considerable waste of resources, loss of energy, and even catastrophic accidents worldwide [1]. The service lives of steel structures, such as sea-crossing bridges, are known to be shortened owing to marine corrosion. Unlike the electrochemical corrosion in other corrosive media, seawater can easily induce pitting corrosion owing to the existence of a large number of Cl^- ions, therefore, extensive research has been conducted to improve the pitting corrosion resistance of metallic materials [2]. Among them, hot-dipped metallic coatings, such as Al and Zn coatings, exhibit superior and long-term corrosion protection owing to the mechanism of physical barrier protection and sacrificial anode-based cathodic protection [3−5]. The corrosion resistance of hot-dipped Al coated steels has been proven to be much higher than that of hot-dipped Zn coated steels [5,6]. Moreover, Al coating is easily available and eco-friendly [7]. Hence, hot dip aluminizing (HDA) is a potential anti-corrosion technology.

In general, an intermetallic compound layer comprising the inner layer of large columnar Fe_2Al_5 and outer layer of a small quantity of $FeAl_3$ is formed at the interface of the molten Al/solid steel induced by the interdiffusion of Al and Fe atoms during HDA. Notably, these Al-rich intermetallic compounds, as well as the original top Al layer, can

Corresponding author: Xian-man ZHANG, Tel: +86-898-66267372, E-mail: xianman213@163.com
DOI: 10.1016/S1003-6326(23)66200-4

be transformed into Fe-rich phases; the types of these compounds are dependent on the holding temperature and time during the appropriate thermal diffusion treatment (TDT) [8,9]. More specifically, the Al atoms in Al-rich aluminides, such as Fe_2Al_5 and $FeAl_3$, can leach out and continue to diffuse inward as an Al source and react with the Fe matrix, thereby resulting in the formation of Fe-rich aluminides, such as $FeAl_2$, FeAl and Fe(Al). Furthermore, an interesting periodic layered structure (PLS) was formed at the $(Cr, Fe)_2B$/Al interface when Fe−Cr−B cast steels were immersed in molten Al, as reported in our previous study [10−12].

Currently, the corrosion resistance of the Fe-rich phases formed during TDT in a Cl^- environment is a highly debated topic in the literature. WANG et al [13] discovered that the corrosion resistance of TWIP steel was substantially improved using HDA with subsequent TDT, whereas excessive TDT, which led to the formation of undesirable intermetallic compounds, decreased the corrosion resistance. There are several important studies on the overall electrochemical corrosion behavior of bulk Al, Zn, and Mg alloys in a NaCl solution which are relevant for the coatings investigated in this study [14−16]. Generally, the role of the second phase that would be intermetallic compounds, in the process of corrosion mainly includes acting as a corrosion barrier and imparting the micro-galvanic effect [17−19]. However, the corrosion behaviors of the layers of intermetallic compounds formed during HDA are easily ignored because their thicknesses are lower than those of the coatings formed by Al and its alloys. This Fe−Al intermetallic compounds layer was anticipated to provide a second line of defence against corrosion when the top Al layer was corroded completely.

Unfortunately, dedicated literature on the corrosion behaviors and dependability of HDA and TDT coatings on steel in a NaCl solution remains scarce. This indicates that more research is required on the electrochemical behavior of the coating/steel system. Hence, in this study, a special Fe−Al intermetallic compound coating with an embedded PLS was fabricated using HDA and subsequent TDT of Fe−Cr−Si−B cast steel. Next, the corrosion behavior of this complex microstructural coating in a 5 wt.% NaCl solution was investigated to provide a new methodology for marine anti-corrosion. The nature of stable corrosion products is the determinant factor for long-term corrosion resistance [20]. Therefore, the corrosion products will not be investigated in this study owing to corrosion being short-term. In addition, the oxide protective film formed on the coating surface was negligible because of the rigorous breakdown induced by the high concentration of Cl^- in the NaCl solution used in this study.

2 Experimental

2.1 Preparation of Fe−Cr−Si−B cast steel

Y-block Fe−Cr−Si−B cast steel was prepared using 250 kg-capacity medium-frequency induction furnace. The charge materials included ferrous alloys such as Fe−32wt.%B, Fe−70wt.%Cr, Fe−20wt.%Si, and clean A3 steel. The Fe−32wt.%B alloy was added to molten metal by pressing before pouring the steel melt into a sodium-silicate CO_2-bonded sand mould at 1500 ℃. The chemical compositions of the Fe−Cr−Si−B cast steel were analysed using inductively coupled plasma atomic emission spectroscopy. The results are listed in Table 1. Test samples with dimensions of 60 mm × 10 mm × 4 mm were cut from the centre of Y-type ingots using wire-electrode cutting.

Table 1 Chemical composition of Fe−Cr−Si−B cast steel (wt.%)

Cr	B	Si	C	Fe
14.7	8.5	10.9	0.9	Bal.

2.2 HDA and TDT

The samples were subjected to standard grinding before being dipped into molten pure Al (3.5 kg) at 750 ℃ for 15 min with the upper end of the specimens fixed using steel wire. After a fixed duration, the samples were withdrawn from the Al melt and cooled in the air to room temperature. Thereafter, TDT of the dipped specimens was performed in a resistance furnace at 750 ℃ for 2 and 8 h, respectively. The specimens diffusion heat-treated for 2 and 8 h were designated as TDT-2 and TDT-8, respectively.

2.3 Immersion test

The specimens treated with HDA and

subsequent TDT were exposed to a 5 wt.% NaCl solution for a static corrosion test, which was conducted at set temperatures of 30 and 60 ℃ in a constant-temperature water tank to evaluate the corrosion behaviors of coatings. To prevent the galvanic corrosion, a section of the specimen with a hole was fixed on a container by threading a rope through it.

2.4 Characterization of coating before and after corrosion

The surface and cross-sectional morphologies and elemental distributions before and after immersion corrosion were investigated using scanning electron microscopy (SEM, Verios G4 UC) coupled with energy dispersive spectroscopy (EDS) and an electron probe micro-analyser (EPMA, JXA−8230) with wavelength dispersive X-ray after standard polishing without etching. Measuring the content of B in boride was difficult because of its small atomic number. Therefore, three-dimensional atom probe tomography (3DAP; LEAP 5000XR) was also conducted. The phase morphologies and distributions were observed using the SEM with back-scattered electron (BSE) and secondary electron (SE) detectors. The bright and dark areas in the mode of BSE represented the large and small average atomic number, respectively. Additionally, the corrosion morphology was clearly observed in the SE mode. The 3DAP specimens of the coatings were prepared using a focused ion beam (FIB, Helios NanoLab 600) by applying a "lift-out" technique.

3 Results and discussion

3.1 Microstructure of Fe−Cr−Si−B cast steel

The microstructure of the Fe−Cr−Si−B cast steel is exhibited in Fig. 1. The tested cast steel comprised four phases including α-Fe(Si) matrix in the white area, Fe−Si phase (Fe_3Si) in the grey area, coarse primary boride in the dark grey area and Si particle in the black area, as shown in Fig. 1. The presence of Fe_3Si phases and Si particles were owing to the limited solid solubility of Si in α-Fe during solidification according to the ternary Fe−Si−B system [21]. The Si particles segregated into the matrix at last. The elemental distribution was analysed using EPMA, as shown in Fig. 2. The results revealed that the distribution of B and Cr coincided, but was obviously opposite to that of Fe and Si. In the region without borides, the distribution of Fe and Si was also completely opposite. Additionally, Cr and B were almost completely distributed in the borides. Furthermore,

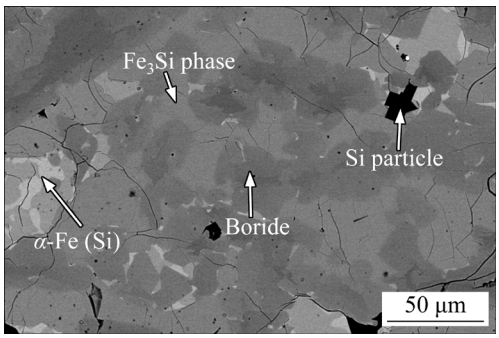

Fig. 1 Microstructures of Fe−Cr−Si−B cast steel

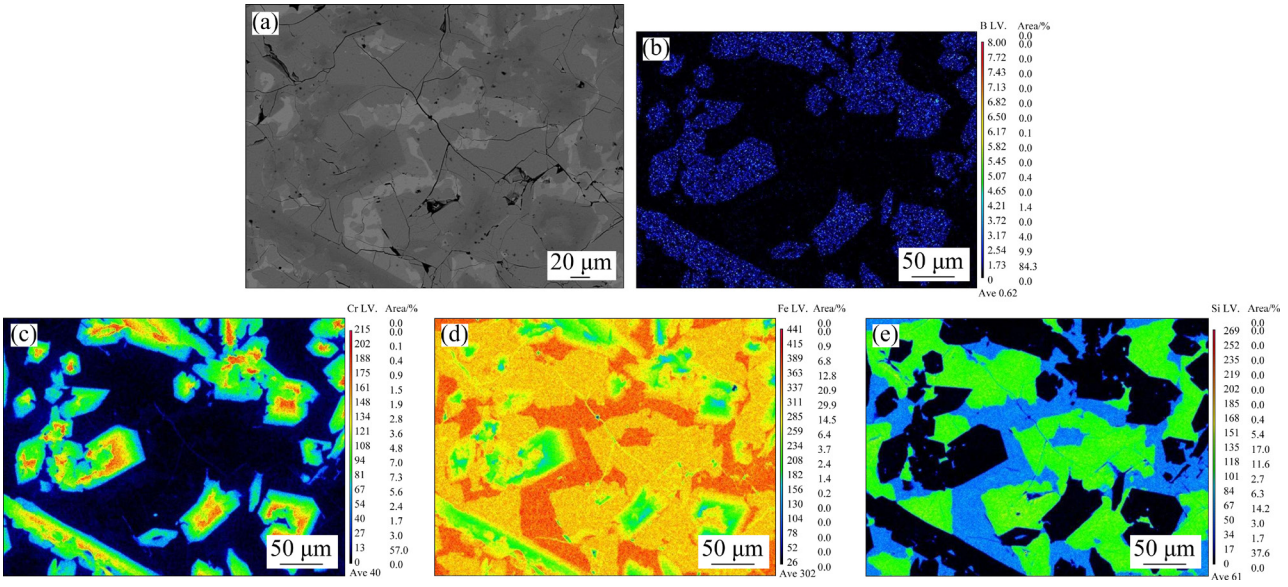

Fig. 2 SEM image (a) and corresponding elemental map analysis of Fe−Cr−Si−B cast steel (b−e)

the concentration of Cr in the boride centre, which acted as the nucleation core during solidification, was much higher than that in the surrounding area. Because the concentration of B in boride is difficult to accurately determine quantitatively using EDS and EPMA, 3DAP was used to further clarify the composition of the boride. The specific concentrations of each constituent element in the bulk of the 3DAP sample were 42.1 at.% B, 24.8 at.% Cr, 33.1 at.% Fe, and a negligible amount of C and Si. In contrast, the compositions of this boride analysed using EPMA were 51.5 at.% B, 11.8 at.% Cr, and 36.7 at.% Fe. Since hydrogen trapping was detected by 3DAP [22,23], so the composition results of the former would be more accurate. The Fe−Cr−B ternary system was complex, because the borides, i.e., CrB, Fe_2B, and Cr_2B, have different elementary cells. Additionally, more than two-thirds of the Cr atoms in Cr_2B can be replaced by Fe, whereas approximately 17 wt.% Fe atoms in Fe_2B can be replaced by Cr [24]. However, the overall Cr content in Fe−Cr−B alloy was reported to be higher than 6.8 wt.%, and the $(Cr, Fe)_2B$ phase was formed [25]. Therefore, $(Cr, Fe)_2B$ and other borides such as (Cr, Fe)B may coexist.

3.2 Interfacial microstructure of HDA

Figure 3 shows the interfacial microstructural morphologies and elemental distributions of Fe−Cr−Si−B cast steel after HDA for 15 min. As shown in Fig. 3, the primary $(Cr, Fe)_2B$ boride had a considerable influence on the interfacial reaction between Fe−Cr−Si−B cast steel and molten Al. As indicated in Figs. 3(a) and (b), unlike the serrated or tongue-like interfacial morphology between the Fe substrate and Fe_2Al_5, the interface between Fe−Cr−Si−B cast steel and the Fe−Al intermetallic compounds layer was smooth. The cross-sectional morphologies were divided into four distinct layers, as shown by the dashed lines in Fig. 3(a). Layer 1 contained the residual Al, Layer 2 was the dissolved layer of Fe−Cr−Si−B cast steel, Layer 3 was the reaction layer, and Layer 4 was the steel substrate. Layers 1 and 2 were separated by a micro-crack, as shown by the arrow in Fig. 3(a). Among these layers, the dissolved Layer 2 often existed only in theory and was difficult to determine quantitatively owing to the inability to determine its original position. However, the borides in the Fe−Cr−Si−B cast steel can be used as an inert marker. Compared with the Fe substrate, these borides were stable in

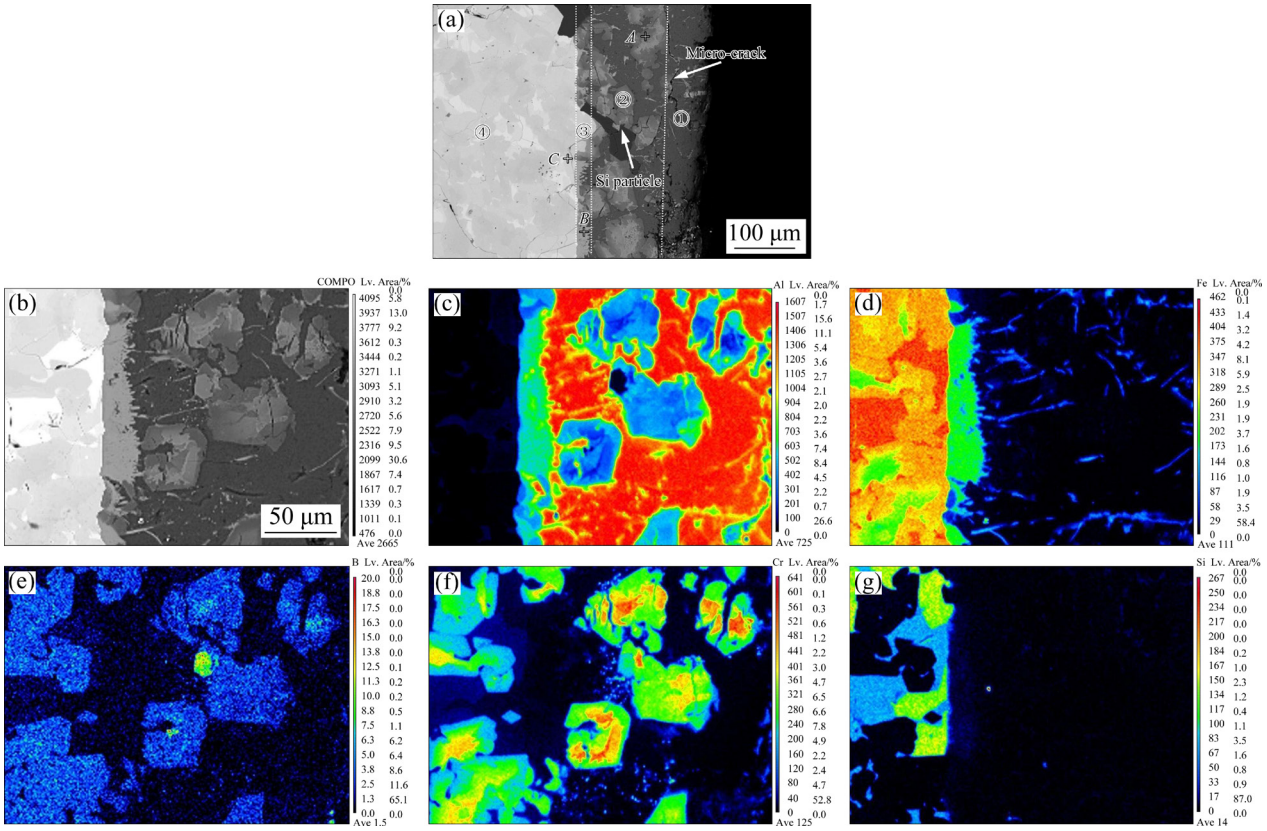

Fig. 3 Cross-sectional morphologies (a) and elemental map analysis of Fe−Cr−Si−B cast steel for hot dip aluminizing of 15 min (b−g)

molten Al to some extent. Thus, while the Fe−Cr−Si−B cast steel was in contacted with the Al melt, the Fe matrix was preferentially dissolved into the Al melt. Subsequently, the areas containing Fe substrate were filled with molten Al (Fig. 3(c)). The block-like borides acted as diffusion barriers and almost retained their morphologies before HDA in the steel except for the presence of micro-cracks caused by the thermal shock of the high-temperature Al melt. Since these micro-cracks were formed during HDA, they were filled with molten Al, as shown in Fig. 3(c). Meanwhile, the boride and Al melt reacted. According to the results of EPMA listed in Table 2, the phases of the product obtained from this reaction for 15 min were hard to identify. Compared with the chemical compositions of this boride in Fe−Cr−Si−B cast steel (see Fig. 2), almost all the Fe atoms in boride selectively dissolved into the Al melt accompanied by the Al atoms added as a result of the diffusion-reaction during HDA. Since the solubility of Al in Cr−B borides was limited [26], this reaction product was donated as B−Cr−Al phase, which was isolated, surrounding by Al.

Table 2 Composition of phases measured using EPMA in Fig. 3(a) (at.%)

Position No.	Fe	Cr	B	Si	Al	Possible phase
A	0.7	17.3	53.2	0.1	28.7	B−Al−Cr
B	23.9	0.3	−	2.3	73.5	$FeAl_3$
C	69.0	1.3	3.9	25.8	−	Fe_3Si

In the Layer 3, the Fe−Al intermetallic compounds dissolved little Si were formed at the α-Fe(Si)/Al interface, as shown in Figs. 3(c, d, g). Furthermore, Fe−Al intermetallic compounds were also formed at the Fe_3Si/Al interface [27]. Notably, according to the results of EPMA listed in Table 2, this Fe−Al intermetallic compound had a stoichiometric ratio of Fe to Al of approximately 3:1; therefore, this compound was identified as $FeAl_3$, which was different from the results obtained from HDA of common steels reported in the literature. The Fe−Al intermetallic compound was also identified as $FeAl_3$ when bulk Fe_2B was hot dipped into molten Al [28]. Moreover, this $FeAl_3$ phase exhibited a favourable columnar crystal structure with the preferred growth direction parallel to the direction of diffusion of the Al atoms [28]. Although the extremely slow growth kinetics of $FeAl_3$ with respect to Fe_2Al_5 was well-known, $FeAl_3$ was the dominant phase formed during the Fe/Al interfacial reaction during HDA of Fe−Cr−B cast steel. The replacement of Fe_2Al_5 by $FeAl_3$ was mainly associated with the influence of the borides contained in Fe−Cr−B cast steel. The corresponding mechanism should attract the attention of researchers. As indicated in Fig. 3(g), the distribution of Si was interesting, except for Si particle (which happened not to exist at the interface in Fig. 3(b), unfortunately, but appeared in Fig. 3(a) and the following figures) which was stable and retained its original morphology, a thin Si-rich film appeared at the matrix/$FeAl_3$ interface with the remaining Si dissolved in the $FeAl_3$ phase. Therefore, the smooth structure at the matrix/$FeAl_3$ interface can be partially attributed to the inhibition effect of Si on the growth kinetics of the Fe−Al compound [29]. However, unlike the formation of the PLSs at the $(Cr,Fe)_2B$/Al interface, no PLSs were observed in the Layer 3, which was mostly attributed to the higher B content in this Fe−Cr−Si−B cast steel than that in our previous study [10−12]. Similar to Layer 2, although morphologies of the borides in Layer 3 were unchanged, their compositions were different from that before HDA with Al added during the reaction between the boride and molten Al. These borides alloyed with Al were the intermediate products of the reaction between $(Cr,Fe)_2B$ and molten Al, which may be thermodynamically unstable.

3.3 Interfacial microstructure of TDT

Figure 4 presents the cross-sectional morphologies of the coating layer after TDT at 750 ℃ for 2 and 8 h. Unlike the morphologies shown in Fig. 3, different phases were formed after TDT. Despite part of the block-like B−Al−Cr phases still being isolated at the sub-surface, a different result was obtained with the appearance of the PLSs. Additionally, the thickness of the intermetallic compounds layer increased with the increase in the duration of TDT owing to the dominant interdiffusion of Fe and Al atoms. More specifically, TDT promoted the conversion of the top Al layer into the Fe−Al intermetallic compounds layer and the fast growth of the aluminide layer. Meanwhile, when the diffusion time was increased to 8 h (Fig. 4(c)), widespread

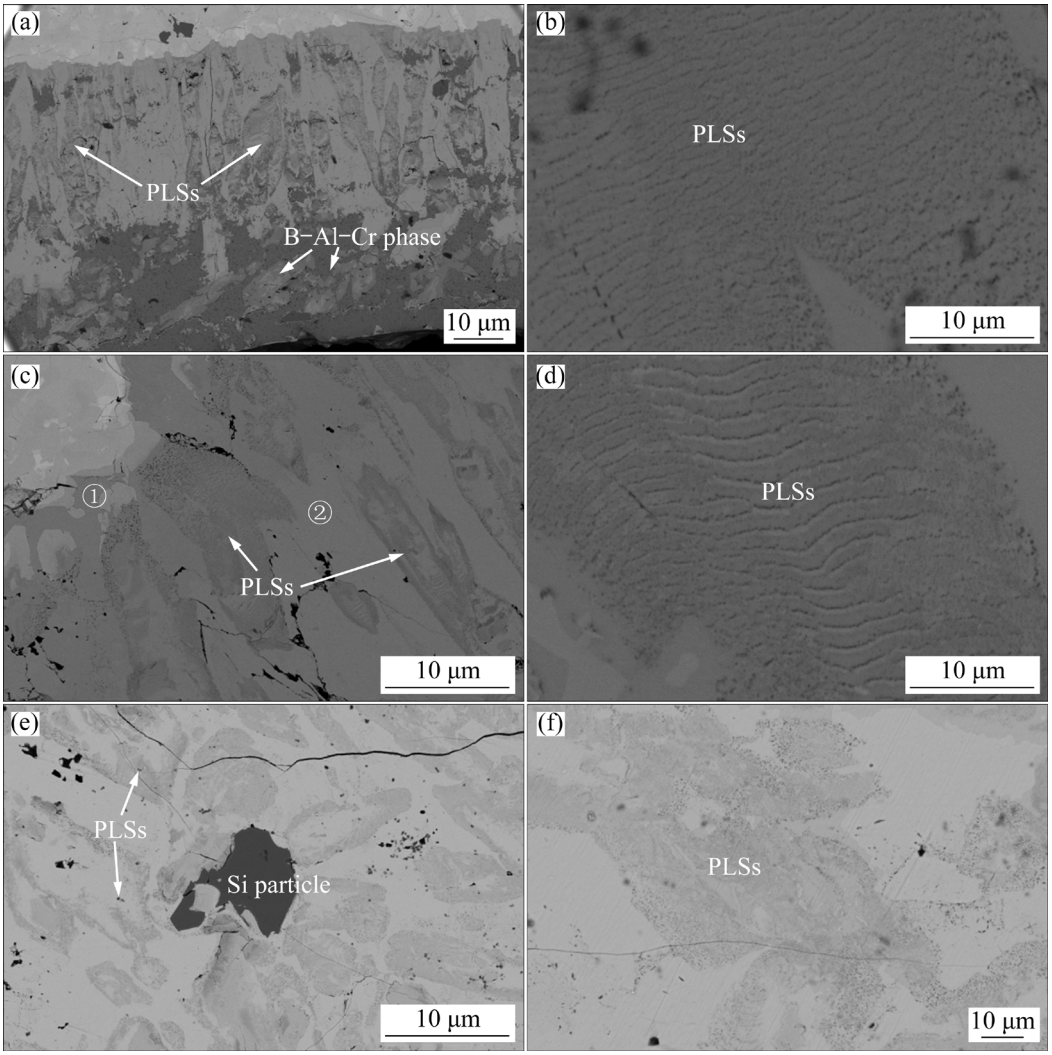

Fig. 4 Morphologies of coating layer after TDT at 750 ℃ for different time: (a, c) Cross-section for 2 and 8 h respectively; (b) High magnification view of PLSs in (a); (d) High magnification view of PLSs in (c); (e) Top-section for 8 h; (f) High magnification view of PLSs in (e)

development of PLSs was noticed; the areas of the PLSs increased and the morphologies became increasingly clear. The nature of TDT was proven to be the same as that of HDA, whereas the results of these treatments were considerably different. The details and mechanisms of these differences will be discussed systematically elsewhere.

The elemental distributions of the PLSs formed in-situ were analysed using EPMA, as shown in Fig. 5. The PLSs were found to consist of two alternating phases: the Cr−Al−B and Fe−Al intermetallic compounds. The EPMA results obtained for the PLSs were in agreement with those obtained from our previous study. The compositions of the PLSs were studied extensively using 3DAP, as displayed in Fig. 6. As shown in Fig. 6, the spatial distribution of B coincided with that of Cr, whereas the spatial distribution of Al coincided with that of Fe and Si. The concentration of elements changed in cycles in the structures of alternating layers. However, these PLSs comprising two alternating phases exhibited a complex spatial structure, and the PLSs were embedded in the Fe−Al intermetallic compounds. The relevant results obtained from the PLSs were confirmed by the comprehensive analysis in the previous study [10−12]. The composition results of Area 1 in Fig. 4 analysed using EPMA were 50.2 at.% Al, 26.6 at.% Fe, 15.4 at.% Si, 4.8 at.% C, 2.2 at.% B, and 0.8 at.% Cr. This result implies that the phase of Area 1 in Fig. 4(c) should be $FeAl_2$ owing to the Al/Fe molar ratio being approximately equal

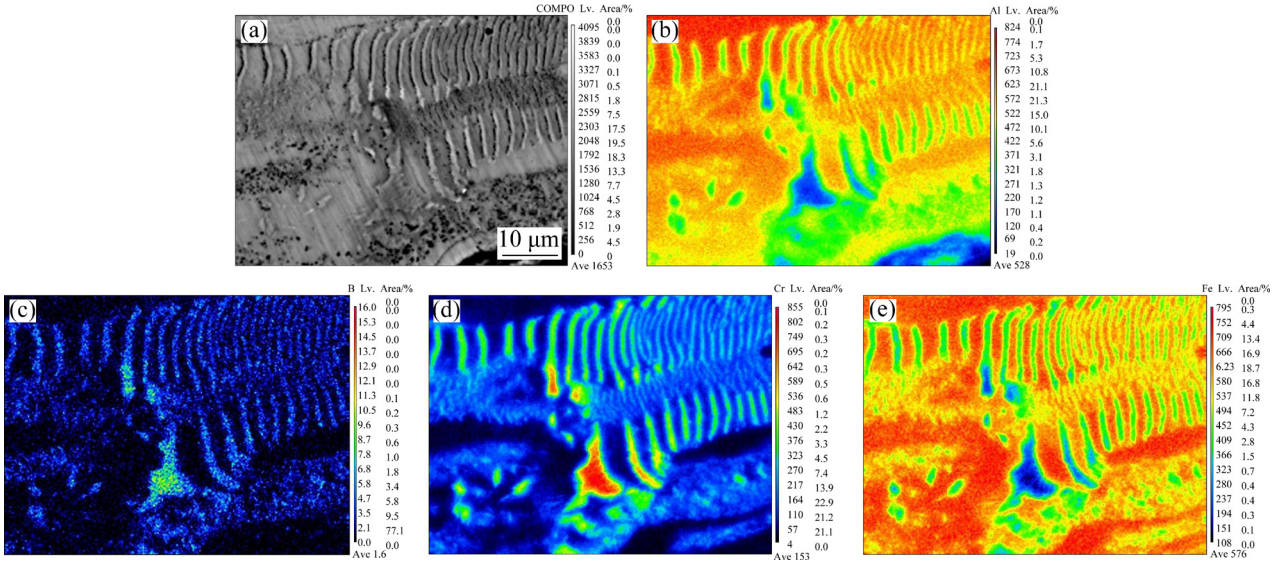

Fig. 5 Elemental map analysis of PLSs

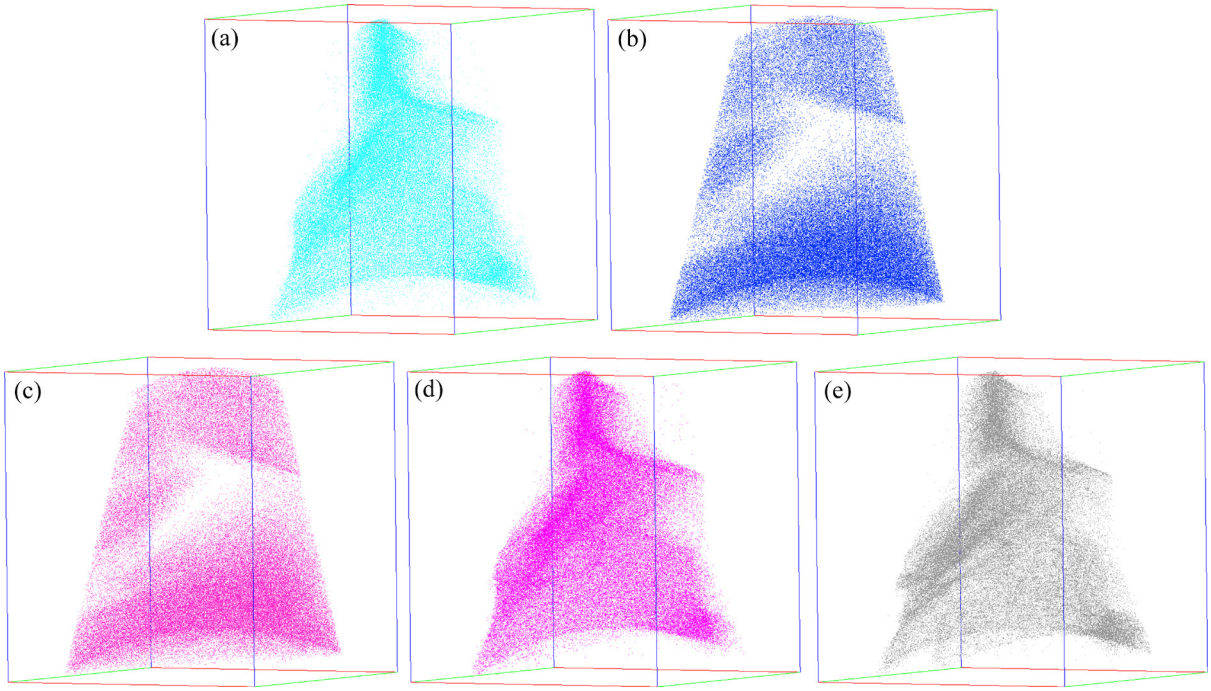

Fig. 6 3DAP analysis of PLSs: (a) Al; (b) B; (c) Cr; (d) Fe; (e) Si

to 2:1. A sub-layer of $FeAl_2$ was formed at the steel substrate/$FeAl_3$ interface owing to the interdiffusion of inwardly diffusing Al atoms and outwardly diffusing Fe atoms during TDT. The phase of Area 2 in Fig. 4(c) was $FeAl_3$. Traces of the Al layer still existed owing to the short reaction time with the steel substrate and relatively low temperature (750 ℃) of TDT-2.

Additionally, as shown in Figs. 4(b) and (c), a considerable number of particles appearing as black dots with nanostructures were clearly observed. These dispersed precipitates were disordered at the initial stage. Eventually, they tended to be non-independent and gradually changed from a disordered dispersion to an ordered arrangement under a certain kind of driving force, which was related to the formation mechanism of PLSs during TDT. The Kirkendall porosity band did not appear in this alloy, and it was severely oxidized instead. The morphologies observed in the top-section view of TDT-8 are shown in Figs. 4(e, f). The lath areas were PLSs, in combination with Figs. 4(c, d). Since

it was the top-section view of the PLSs, the morphologies of two alternating phases as shown in Figs. 4(b, d) did not appear.

3.4 Corrosion interfacial morphology of HDA coating

Figures 7(a) and (b) demonstrate the cross-sectional morphology of the HDA coating layer after immersion in a 5 wt.% NaCl solution for 216 h. The corrosion was observed to progress heterogeneously. The HDA coating layer provided good protection and demonstrated an excellent shielding effect against pitting and galvanic corrosion. The underlying layer of Fe−Al intermetallic compounds did not corrode until the outer Al layer was dissolved completely. A compact corrosion product layer covered on the well-protected surface of the Al layer, as depicted in Figs. 7(c, d), and acted as a barrier for the mass transport of O_2 and dissolved Al^{3+}. Furthermore, no channels existed for Cl^- migration to the fresh alloy surface of the underlying substrate. The compact corrosion product layer effectively inhibited the infiltration of Cl^-. Owing to the short duration of corrosion, the corrosion depth did not reach the Fe−Al intermetallic compounds layer. Thus, TDT was used to consume the outer Al layer in order to study the corrosion behaviors of the Fe−Al intermetallic compounds in a short duration of corrosion.

3.5 Corrosion interfacial morphology of TDT

Figure 8 demonstrates the cross-sectional morphology of the TDT-2 coating layer after immersion in a 5 wt.% NaCl solution for different durations. As mentioned above, a thin Al film remained on the top of the Fe−Al intermetallic compounds. As long as the top Al layer was in direct contact with the corrosive medium, corrosion was effectively retarded. Therefore, the corrosion of the Fe−Al intermetallic compounds layer began only when the Al layer was completely corroded. In addition, several phases coexisted in the intermetallic compounds layer, and the galvanic coupling among them induced pitting corrosion in the periphery of the B−Cr−Al phase and Si particle in the presence of Cl^-. The corrosion depth of the intermetallic compounds layer was considerably different at different places. The B−Cr−Al phases contained in the top Al film also demonstrated superior corrosion resistance and acted as a corrosion barrier to prevent the corrosive medium (Cl^-) from penetrating. Once the corrosion front reached the Fe−Al intermetallic compounds layer, the front changed from the anode to the cathode owing to the difference in the corrosion potential between the Al layer and the Fe−Al intermetallic compounds layer [30−32].

More specifically, the corrosion was initiated and grew along the PLSs because the corrosion

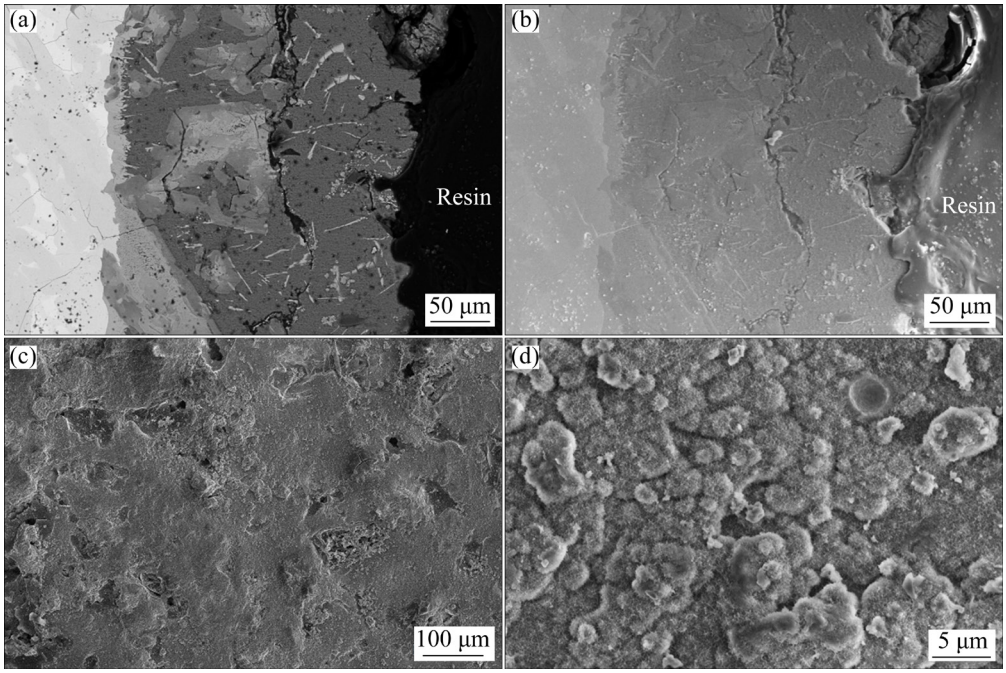

Fig. 7 Corrosion morphology of HDA coating layer after being immersed in 5 wt.% NaCl solution for 216 h: (a) BSE image; (b) SE image; (c) Top-view; (d) High magnification of (c)

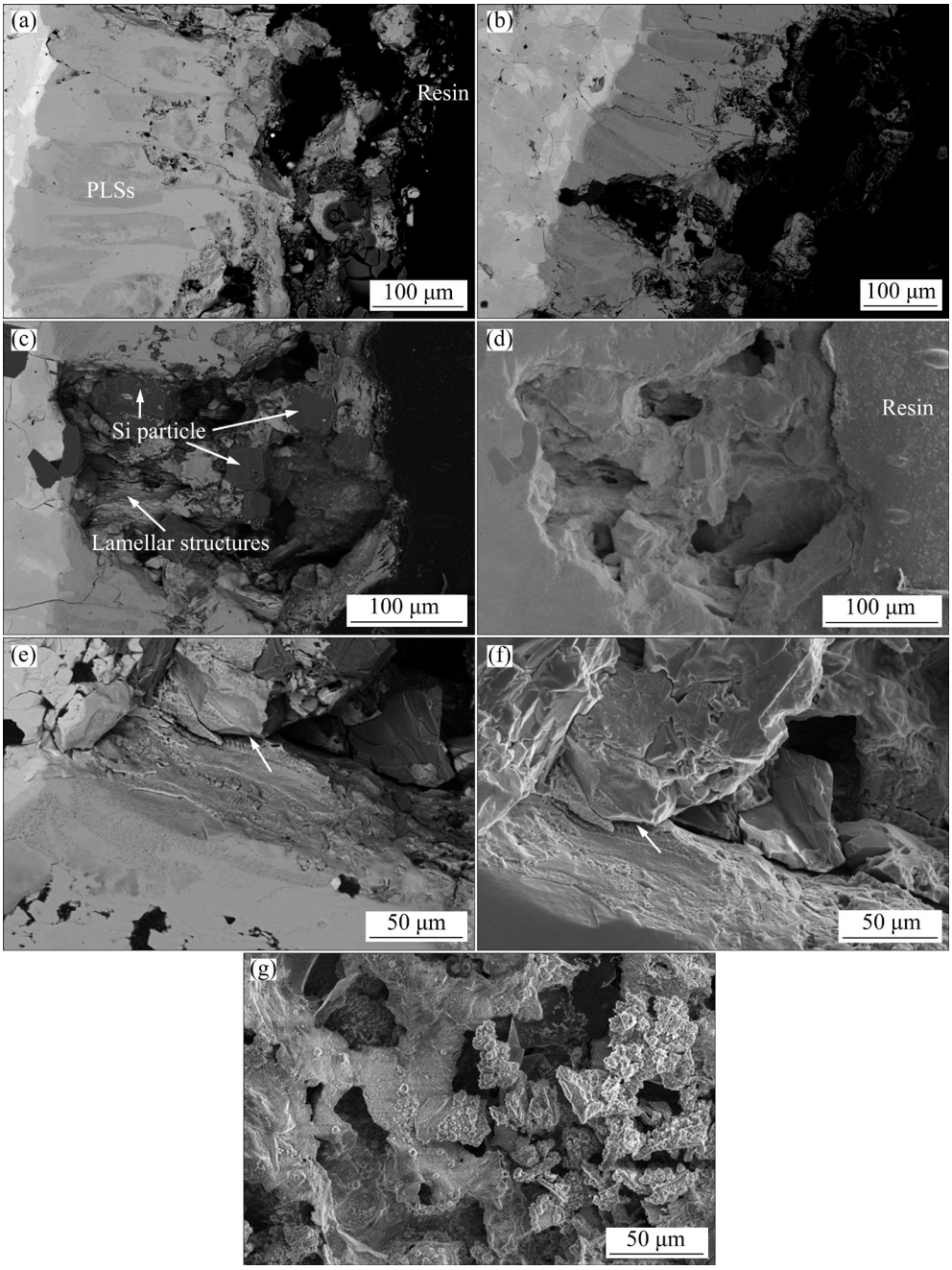

Fig. 8 Corrosion morphology of TDT-2 coating layer after being immersed in 5 wt.% NaCl solution for different time: (a) BSE for 48 h; (b) BSE for 120 h; (c) BSE for 192 h; (d) SE for 192 h; (e) BSE for 216 h; (f) SE for 216 h; (g) Top-view of corrosion surface

potential of the PLSs was more negative than that of the adjacent Fe−Al intermetallic compounds. And the stable Si particles were more inert than the $FeAl_3$ matrix and acted as a cathode [30]. Consequently, the pitting corrosion occurred preferentially at the surround of the Si particles. The galvanic effect of the Si particles was the dominant factor in the corrosion of the TDT coating. Additionally, Si was easily converted to be a SiO_2 protective film, which improved the corrosion resistance in the Cl^- environment [33]. The nobility of the Fe−Al interdiffusion layer was proven to be higher than that of the steel substrate [30]. Therefore, the presence of the Si particles unexpectedly compensated for the defect of the electrochemical corrosion potential of the Fe−Al intermetallic compound and protected the steel substrate.

Furthermore, another type of lamellar structure (shown by the arrow in Fig. 8(c)) was observed.

However, the direction of these lamellar structures was almost perpendicular to that of the PLSs. Additionally, whether these lamellar structures were the PLSs mentioned above was unclear, and therefore, 3DAP was employed to analyze their compositions. The location and results of the 3DAP analysis are shown in Fig. 9. The elemental contents were observed to be uniform throughout the area, and the main constituent elements were Al and Fe, with traces of Si. The specific composition of the bulk in Fig. 9 was 71.5 at.% Al, 23.3 at.% Fe, and 5.2 at.% Si. Thus, the lamellar structures were $FeAl_3$ phase. The formation mechanism of the $FeAl_3$ phase with a lamellar structure during corrosion corresponded to the structural defect of the columnar crystals induced by preferential growth [28,34]. Particularly, a corrosive medium easily penetrated the defects of the columnar structure [35]. However, the presence of the PLSs blocked the pathway of the corrosive medium in the horizontal direction, and the development of localized corrosion was effectively delayed or trapped in the PLSs. The length of the diffusion path of Cl^- was increased by the PLSs. The corrosion protection mechanism of the PLSs was attributed to both the effects of the special periodic interface, which allowed the lateral spreading of the corrosive agent rather than directional penetration

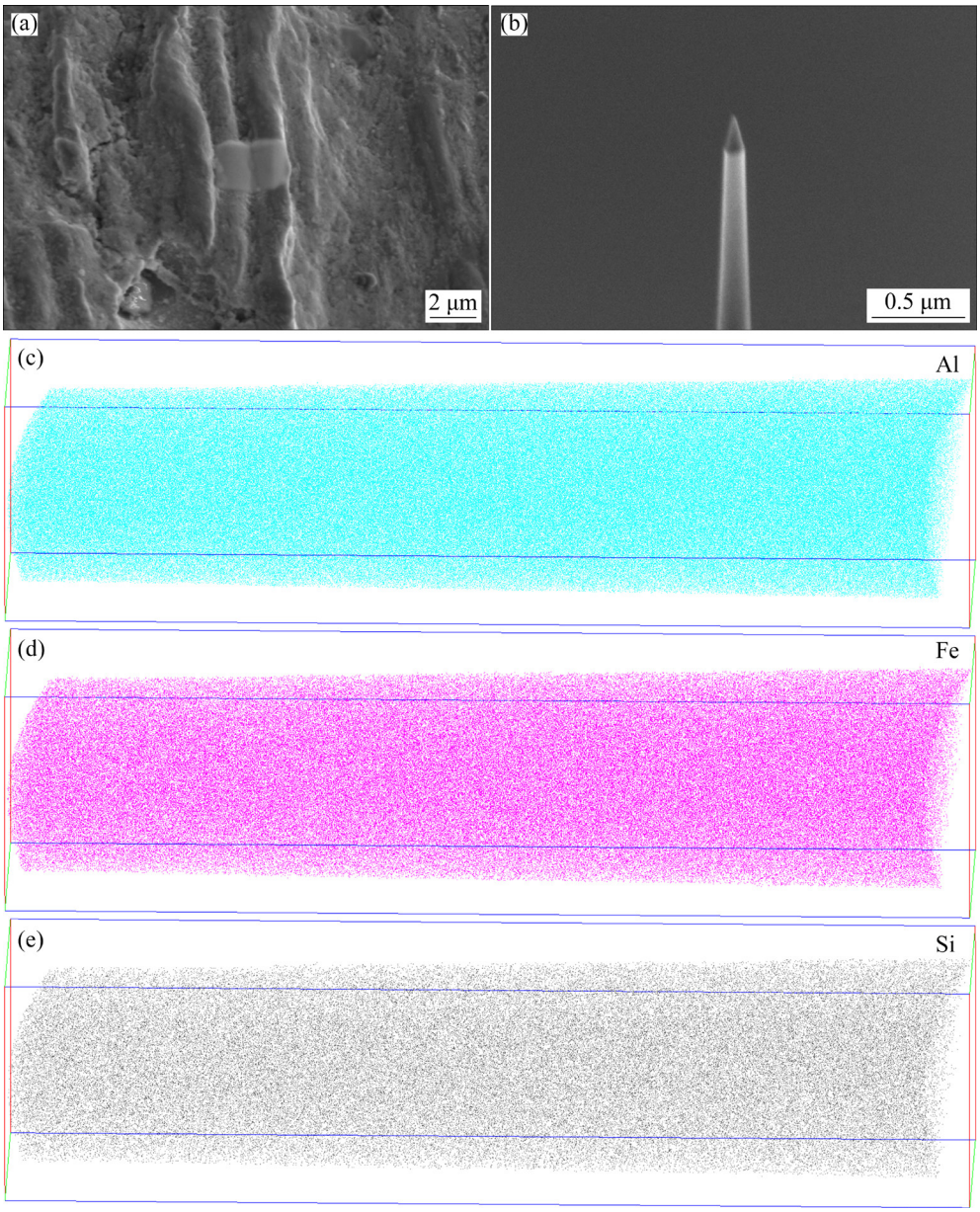

Fig. 9 3DAP analysis of lamellar structure: (a) Location of sample; (b) Overview of reconstructed sample; (c) Al; (d) Fe; (e) Si

into the substrate. Additionally, the micro-galvanic coupling occurred between the two alternating phases contained in the PLSs [36−38]. However, the PLSs were eventually corroded by Cl^- owing to the micro-galvanic effect. The corroded PLSs were clearly visible, and an anisotropic corrosion behavior was observed, as shown by the arrows in Figs. 8(e) and (f). A drawback of the PLSs was their limited lateral length. This dual effect of the PLSs formed in-situ is expected to be used in its entirety to improve the corrosion resistance of the underlying matrix in the near future. With the increase in the immersion time, the corrosion front gradually extended to the substrate/Fe-Al intermetallic compounds, as demonstrated in Figs. 8(e) and (f), and the width of the pit increased.

In contrast, the corrosion surface was porous, as shown in Fig. 8(g), which was caused by anodic dissolution. The loose film of the corrosion product acted as the corrosion channel and promoted the rapid penetration of Cl^- into the fresh sub-layer.

The average corrosion rate of the TDT-2 coating is shown in Fig. 10. The evolution of the depth and width of the pit within the set corrosion time were used to characterize the average vertical and horizontal corrosion rates of the TDT sample, respectively. The vertical corrosion rate was observed to decrease sharply, and the horizontal corrosion rate increased slightly. Eventually, both of the corrosion rates were stable at different levels.

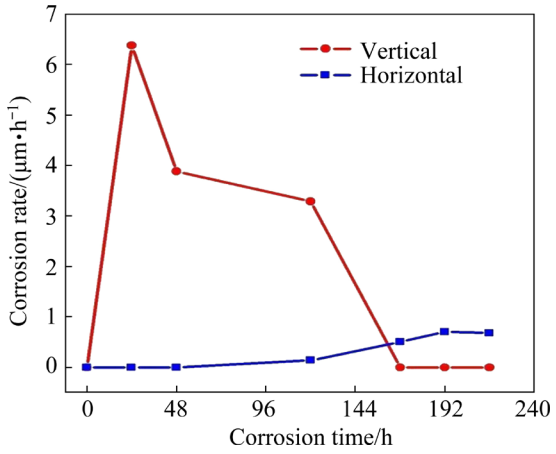

Fig. 10 Average corrosion rate of TDT-2 coating

Figure 11 shows the cross-sectional morphologies of the TDT-8 coating layer after immersion in a 5 wt.% NaCl solution for different durations. The first impression was that the depth of corrosion of TDT-8 was much greater than that of TDT-2 owing to the absence of the sacrificial protection offered by the Al overlay. As already outlined, the Si particles were stable and maintained their original morphologies during the corrosion process. With an increase in the exposure time, the corrosion depth gradually increased. The lamellar structures were observed again at the corroded interface. Additionally, some cube-shaped phases appeared, and therefore, elemental mapping was performed in the region enclosed within the dashed lines in Fig. 11(e). The results are shown in Fig. 12. The results showed that the cube-shaped phases were Fe−Al intermetallic compounds. Especially, the presence of O and Cl further confirmed that this area was corroded. The previous results showed that the PLSs acted as the anode and corroded preferentially owing to the galvanic effect. On the other hand, PLSs improved the barrier properties by creating traps for Cl^- by prolonging the diffusion path. Therefore, PLSs were only slightly permeable by the corrosive solution unlike that of the monolayer. Unlike the top-view morphologies of the corroded TDT-2 shown in Fig. 8(g), a dense layer of corrosion products with larger voids was observed in Fig. 11(g), which was related to the evolution of the phases during TDT, as described in Section 3.3. Overall, although different phases manifested different corrosion behaviors, the TDT coating layer served as a barrier to obstruct the corrosion from extending into the steel substrate. The steel substrate retained its cathodic protection until the Fe−Al intermetallic compounds layer was corroded completely [6].

The average corrosion rate of the TDT-8 coating layer is shown in Fig. 13, which is similar to that of TDT-2, as shown in Fig. 10. The horizontal corrosion rate did not reach the stable state, and was still increasing, which was ascribed to the larger thickness of PLSs and Fe−Al intermetallic compounds layer introduced by increasing the duration of TDT.

Figures 14 and 15 show the corrosion interfaces of the coating layer after TDT at 60 ℃ for 2 h. The presence of O indicated that corrosion occurred in these areas, as shown in Fig. 15(g). Additionally, the high temperature of the NaCl solution had a major influence on the corrosion rate. With the increase in the corrosion temperature, the corrosion depth of TDT at 60 ℃for 2 h was

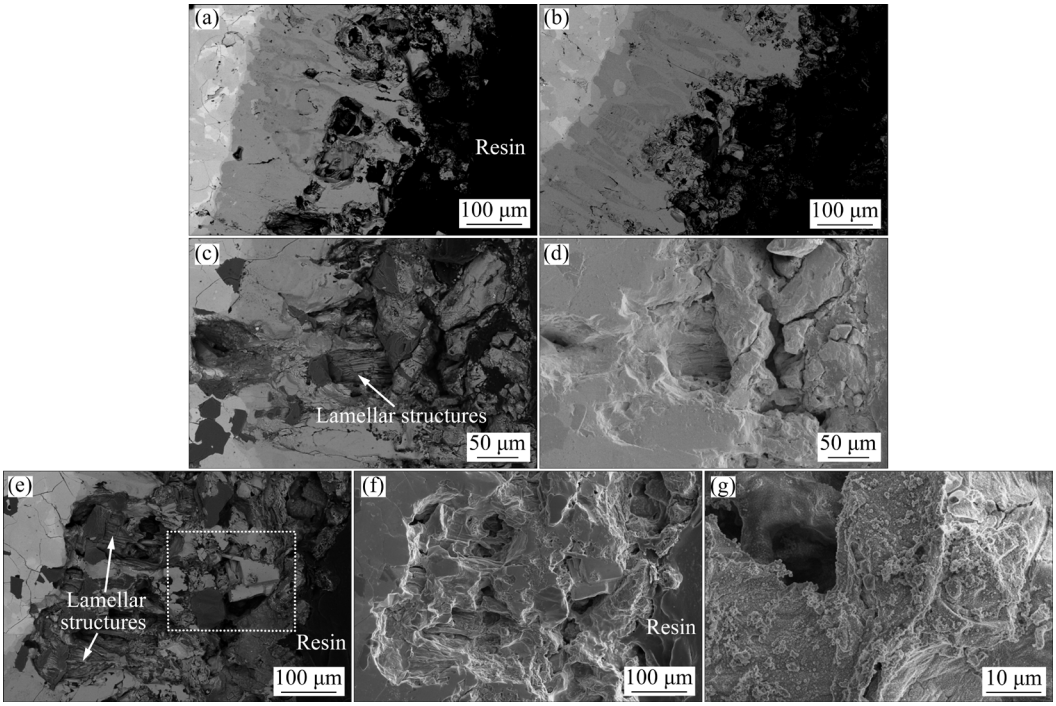

Fig. 11 Corrosion morphology of TDT-8 coating layer after being immersed in 5 wt.% NaCl solution for different time: (a) BSE for 48 h; (b) BSE for 120 h; (c) BSE for 192 h; (d) SE for 192 h; (e) BSE for 216 h; (f) SE for 216 h; (g) Top surface

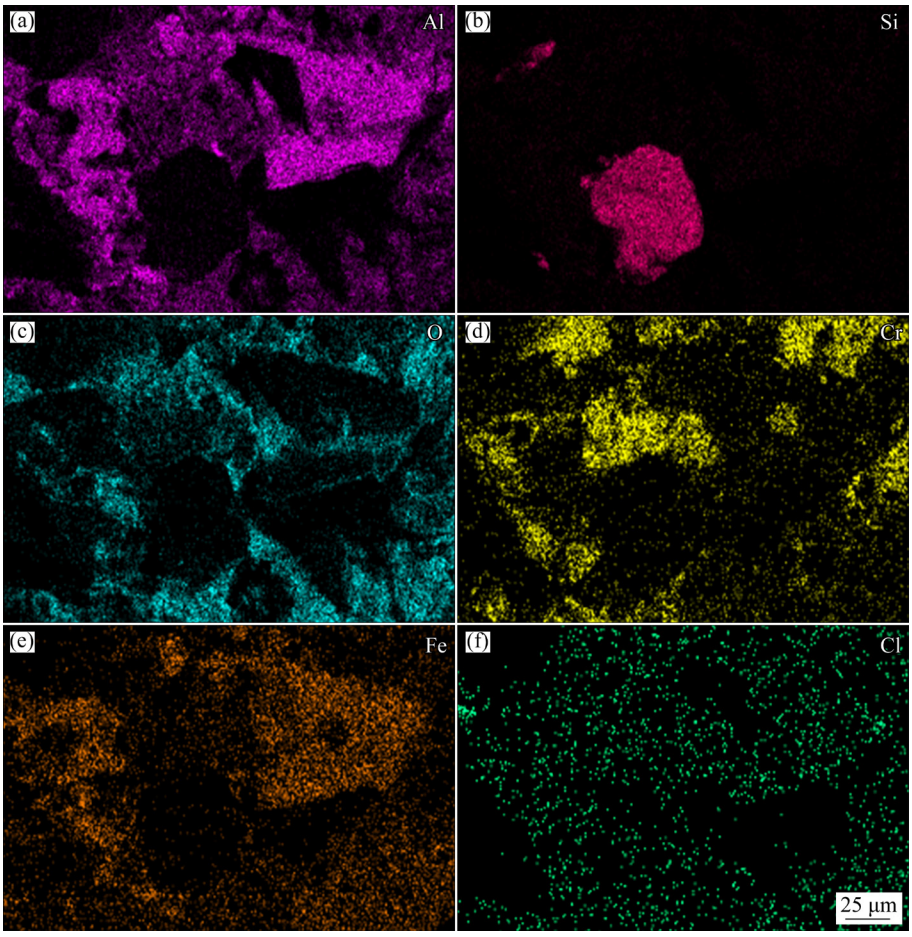

Fig. 12 Elemental map analysis of region enclosed within dashed lines in Fig. 11(e)

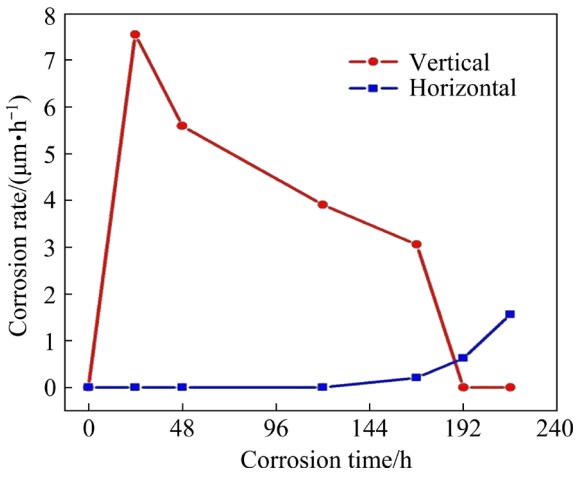

Fig. 13 Average corrosion rate of TDT-8 coating layer

approximately equal to that of TDT at 30 ℃ for 120 h. As indicated above, an Al film was coated on the top of the TDT-2 specimen, which exhibited sacrificial anodic protection (Fig. 14). The results of elemental map analysis of the corroded interface of TDT-2 in a 5 wt.% NaCl solution at 60 ℃ for 2 h, as shown in Fig. 15, revealed that the stable block-like B−Al−Cr phases were present. The results of EPMA revealed that the compositions of this B−Al−Cr phase (as shown by the arrow in Fig. 15(a)) were 56.3 at.% B, 19.2 at.% Al, 15.9 at.% Cr, 2.3 at.% Fe, and 2.1 at.% Si. Unlike the compositions of the B−Al−Cr phase formed during HDA, as listed in Table 2, some of the Al was selectively leached from the B−Al−Cr phase, thereby leading to the quantity of Al being smaller than that before corrosion. The selectively leached Al, which facilitated the formation of a protective Al_2O_3 film [39], contributed to the corrosion resistance of the B−Al−Cr phase.

Complementary to the microstructural evolution of TDT, more details were revealed at the interface of the steel/intermetallic compounds in Fig. 15. As shown in Fig. 15(b), a multi-layered structure with a complex mixture of PLSs, $FeAl_3$, $FeAl_2$, and even FeAl or Fe(Al) was formed owing to the inward diffusion of Al towards the α-Fe(Si) phase and outward diffusion of Fe atoms. More specifically, the interdiffusion of Al and Fe occurred during TDT, thereby resulting in a transformation of the phase and a change in concentration distribution. A Fe-depleted film appeared at the diffusion front of $(Cr, Fe)_2B$/PLSs owing to the selective dissolution of Fe from $(Cr, Fe)_2B$ during the early stage of the $(Cr, Fe)_2B$/Al reaction, which was consistent with the observations from our previous study [10−12], as shown in Fig. 15(c).

To further interpret the corrosion behavior and better understand the corrosion mechanism of the TDT coating, the top-sectional morphologies of the TDT-8 coating layer after immersion in a 5 wt.% NaCl solution for 4 h are shown in Fig. 16.

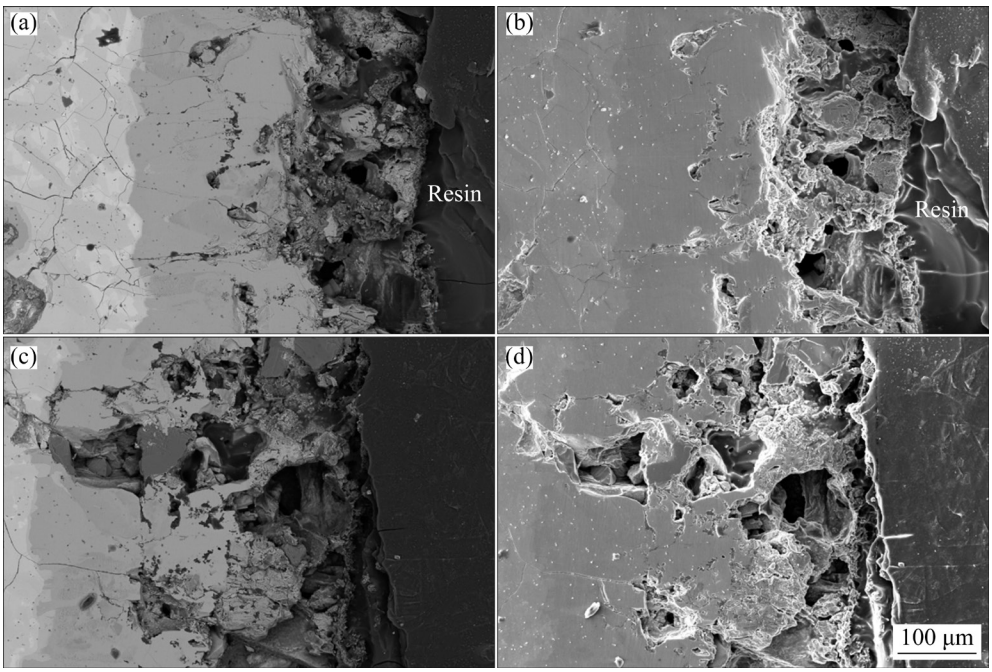

Fig. 14 Corrosion interfaces of coating layer after TDT at 60 ℃ for 2 h: (a) BSE and (b) SE for TDT-2; (c) BSE and (d) SE for TDT-8

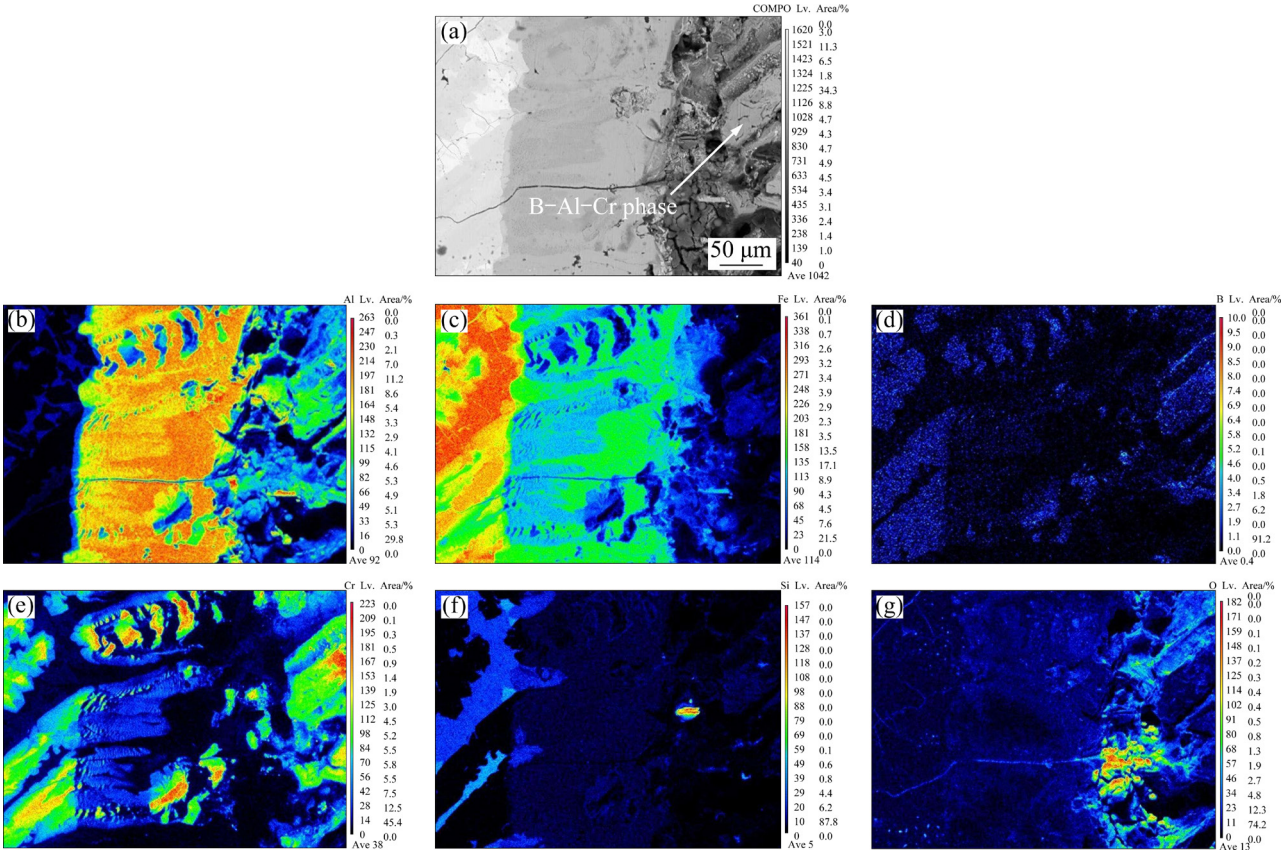

Fig. 15 Elemental map analysis of corroded interface of TDT-2 in 5 wt.% NaCl solution at 60 ℃for 2 h

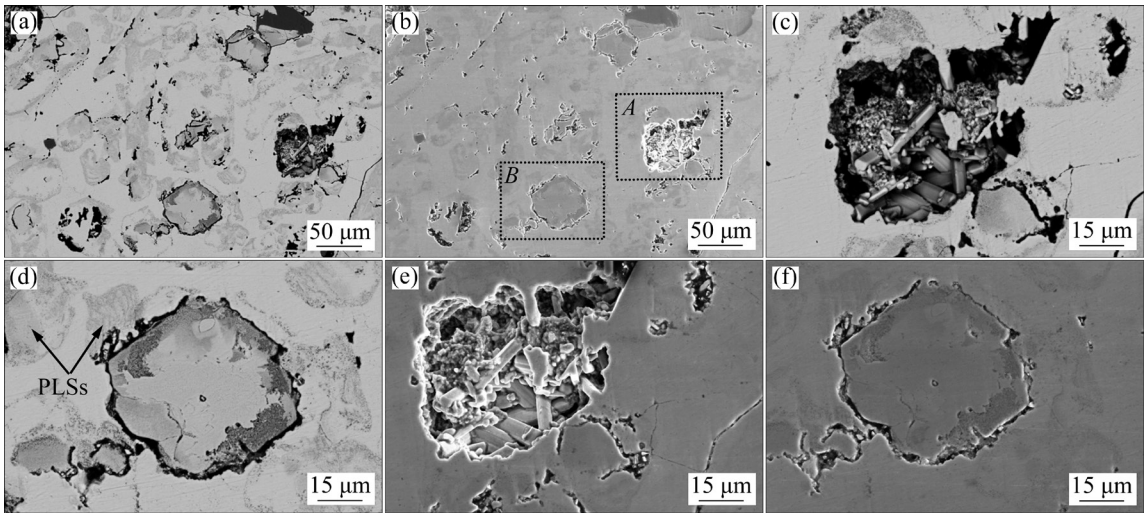

Fig. 16 Top-sectional morphology of coating layer after TDT-8 at 60 ℃ for 2 h: (a) BSE and (b) SE for TDT-8; (c, d) Magnified images of dotted-boxed Regions *A* and *B* in (b), respectively; (e, f) SE of (c, d), respectively

Furthermore, Fig. 17 and Table 3 exhibit the EPMA results. The filiform corrosion mode was observed. The difference in the corrosion potential between the Si particles and PLSs and Fe−Al intermetallic compound matrix resulted in the localized corrosion. Pitting began at the interface between the B−Al−Cr phase and $FeAl_3$. As the corrosion progressed, the localized corrosion did not propagate from the Fe−Al intermetallic compound but started at the adjacent interface of the block-like B−Al−Cr phases. The Fe−Al intermetallic compound was the $FeAl_3$ phase, which was in good agreement with the

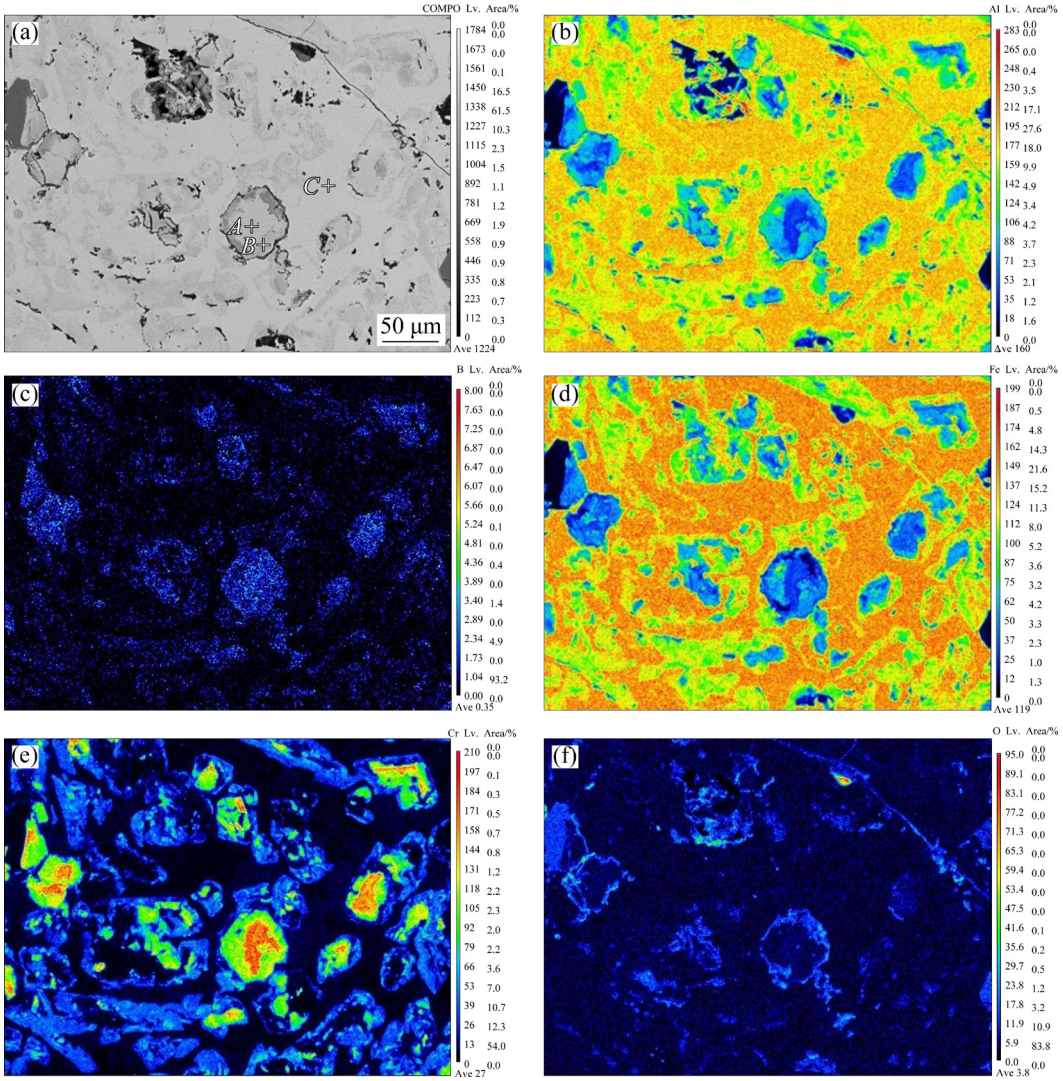

Fig. 17 Element maps of top-sectional TDT-8 coating layer after being immersed in 5 wt.% NaCl solution for 4 h

Table 3 Composition of phases measured using EPMA in Fig. 17(a) (at.%)

Position No.	Fe	Cr	B	Si	Al	Possible phase
A	3.2	24.6	62.8	0.6	8.8	B−Al−Cr
B	5.2	17.3	60.3	1.0	16.2	B−Al−Cr
C	23.4	1.0	7.6	4.3	63.7	$FeAl_3$

results listed in Table 2. The PLSs, which demonstrated superior corrosion resistance, existed stably in an irregular morphology, as seen in the top-sectional view. At the bottom of the corrosion pit, typical columnar $FeAl_3$ phases appeared

All the results presented above highlighted the special microstructural features and corrosion behavior of Fe−Cr−Si−B cast steel treating with HDA and TDT. When Fe−Cr−Si−B cast steel was dipped into an Al melt, a large amount of dissolution occurred on the surface of the α-Fe(Si) and Fe_3Si phases contained in the cast steel in the early state of exposure to molten Al. Additionally, the residual $(Cr, Fe)_2B$ boride skeletons incompletely reacted with the Al melt after a period of incubation. Owing to the limited reaction time, an intermediate product designated as the B−Al−Cr phase was formed, which eventually formed the PLSs as the TDT duration was increased. Instead of Fe_2Al_5, $FeAl_3$ was subsequently formed at the Fe/Al interface after the early stage of the dissolution of the Fe substrate. During TDT, the dominant interdiffusion between Al and Fe atoms occurred continuously. The thickness of the coating increased as the duration of TDT increased. Since the reaction time was sufficient, the PLSs were formed in-situ at the $(Cr, Fe)_2B$/Al interface. Meanwhile, $FeAl_2$ was formed at the Fe/Al interface owing to the limited

Al resource and holding time. The corrosion of the residual Al layer represented the corrosion behavior of the HDA coating for short-term immersion in the NaCl solution. The Fe−Al intermetallic compounds did not corrode until the outer Al layer was entirely consumed, and TDT had a significant influence on the corrosion behavior of the coating. Localized corrosion preferentially began at the block-like B−Al−Cr phase/$FeAl_3$ interface and propagated along the PLSs. The Si particles were unusually stable throughout the process. Additionally, they acted as a cathode and promoted the corrosion of the adjacent anodic area, the dissolution of which was enhanced by the presence of Cl^-. These behaviors were expected because of the changes in the corrosion potential of the dynamic corrosion front. The corrosion depth of excessive TDT coating was larger than that of the HDA coating. More specifically, excessive TDT lead to the deterioration of the corrosion resistance. The high temperature of the NaCl solution dramatically accelerated the corrosion process. The enhanced corrosion resistance of the Fe−Cr−Si−B cast steel can be ascribed to the combined effects of the physical barrier and sacrificial anode protection of the $FeAl_3$ phases. The appearance of the PLSs improved the capability of $FeAl_3$ phases to sacrificially protect the steel substrate. In the design of advanced anti-corrosion coating for steel, fully optimized PLSs formed in-situ may be considered another promising candidate for forming protective coatings.

4 Conclusions

(1) The dissolution of solid steel into molten Al at the early stage of HDA was observed from the borides contained in Fe−Cr−Si−B cast steel owing to the stable existence of borides in the Al melt in a short time, to some extent. The product obtained from the interfacial reaction between the Fe matrix in Fe−Cr−Si−B cast steel and molten Al was $FeAl_3$ with a columnar crystal structure.

(2) The interfacial reaction between $(Cr, Fe)_2B$ and molten Al, which resulted in the formation of the PLSs, required a period of incubation. Although the PLSs were not formed during HDA owing to the short duration of hot dipping, they appeared during the subsequent TDT.

(3) The corrosion behavior of the residual Al layer resembled that of the HDA and TDT coatings over a short duration till the Al coating was consumed completely. The thick TDT coating resulted in the promoted corrosion of the PLSs and $FeAl_3$ owing to both of the presence of the cathodic effect of the Si particle and the absence of the sacrificial anode protection of the Al layer. The steel substrate retained its cathodic protection until the Fe−Al intermetallic compounds layer was corroded completely.

(4) Localized corrosion caused by Cl^- preferentially began at the block-like B−Al−Cr phase/$FeAl_3$ interface and propagated along the PLSs. The Si particle acted as the cathode and promoted the corrosion process of $FeAl_3$ and PLSs, thereby protecting the steel substrate. Additionally, the corrosion attack in the NaCl solution with an elevated temperature was severe.

Acknowledgments

The authors appreciate the financial support from the Natural Science Foundation of China (Nos. 42066003, 51701053), General Program of Natural Science Foundation of Hainan (Nos. 420RC522, 521RC503, 517076), Central Government Guiding Special Funds for the Development of Local Science and Technology, China (No. ZY2018HN09-6), Opening Project of Shanghai Synchrotron Radiation Facility, China (Nos. 2018-SSRF-PT-003860, A01202001004) and Guangdong Key Laboratory for Advanced Metallic Materials Processing (South China University of Technology), China (No. GJ201609).

References

[1] LI X G, ZHANG D W, LIU Z Y, LI Z, DU C W, DONG C F. Materials Science: Share corrosion data [J]. Nature, 2015, 527: 441−442.

[2] ZHANG X M, CHEN Z Y, LUO H F, ZHOU T, ZHAO Y L, LING Z C. Corrosion resistances of metallic materials in environments containing chloride ions: A review [J]. Transactions of Nonferrous Metals Society of China, 2022, 32(2): 377−410.

[3] LIU W, Li M C, LUO Q, FAN H Q, ZHANG J Y, LU H S, CHOU K C, WANG X L, LI Q. Influence of alloyed magnesium on the microstructure and long-term corrosion behavior of hot-dip Al−Zn−Si coating in NaCl solution [J]. Corrosion Science, 2016, 104: 217−226.

[4] RAI P K, ROUT D, SATISH KUMAR D S, SHARMA S, BALACHANDRAN G. Effect of magnesium on corrosion behavior of hot-dip Zn−Al−Mg coating [J]. Journal of

Materials Engineering and Performance, 2021, 30(6): 4138−4147.

[5] PRADHAN D, MONDAL A, CHAKRABORTY A, MANNA M, DUTTA M. Microstructural investigation and corrosion behavior of hot-dipped Al−Si−Mg−Cu alloy coated steel [J]. Surface and Coatings Technology, 2019, 375: 427−441.

[6] KAINUMA S, YANG M Y, GAO Y, HASHIMOTO M. Long-term deterioration mechanism of hot-dip aluminum coating exposed to a coastal-atmospheric environment [J]. Construction and Building Materials, 2021, 280: 122516.

[7] LEMMENS B, GARCIA Y G, CORLU B, de STRYCKER J, de GRAEVE I, VERBEKEN K. Study of the electrochemical behaviour of aluminized steel [J]. Surface and Coatings Technology, 2014, 260: 34−38.

[8] MUHAMMED H J, BENKE M, KONCZ-HORVÁTH D, SÁLYI Z, TÖRÖK T I. Characterization of hot-dip aluminized C45 carbon steel before and after cyclic heating in air [J]. Surface Engineering and Applied Electrochemistry, 2021, 57(4): 431−438.

[9] HUILGOL P, UDUPA K R, BHAT K U. Microstructural investigations on the hot-dip aluminized AISI 321 stainless steel after diffusion treatment [J]. Surface and Coatings Technology, 2019, 375: 544−553.

[10] ZHANG X M, CHEN W P, LUO H F, LING Z C, WANG J, ZHOU T, LI S Y. Influence of Cr on the interfacial boride reaction between Fe−Cr−B cast steel and molten aluminium [J]. Corrosion Science, 2019, 158: 108098.

[11] ZHANG X M, CHEN W P, LUO H F, LI S, ZHOU T, SHI L Y. Corrosion resistance and interfacial morphologies of novel Fe−Cr−Mo−B cast steels in molten aluminum [J]. Corrosion Science, 2017, 125: 20−28.

[12] ZHANG X M, CHEN W P, LUO H F, ZHOU T. Formation of periodic layered structure between novel Fe−Cr−B cast steel and molten aluminum [J]. Scripta Materialia, 2017, 130: 288−291.

[13] WANG W, WANG D, HAN F S. Improvement of corrosion resistance of twinning-induced plasticity steel by hot-dipping aluminum with subsequent thermal diffusion treatment [J]. Materials Letters, 2019, 248: 60−64.

[14] VERMA C, EBENSO E E, QURAISHI M A. Corrosion inhibitors for ferrous and non-ferrous metals and alloys in ionic sodium chloride solutions: A review [J]. Journal of Molecular Liquids, 2017, 248: 927−942.

[15] SUN Y W, PAN Q L, SUN Y Q, WANG W Y, HUANG Z Q, WANG X D, HU Q. Localized corrosion behavior associated with Al_7Cu_2Fe intermetallic in Al−Zn−Mg−Cu−Zr alloy [J]. Journal of Alloys and Compounds, 2019, 783: 329−340.

[16] PROSEK T, HAGSTRÖM J, PERSSON D, FUERTES N, LINDBERG F, CHOCHOLATÝ O, TAXÉN C, ŠERÁK J, THIERRY D. Effect of the microstructure of Zn−Al and Zn−Al−Mg model alloys on corrosion stability [J]. Corrosion Science, 2016, 110: 71−81.

[17] MA H, CHEN X Q, LI R H, WANG S L, DONG J H, KE W. First-principles modeling of anisotropic anodic dissolution of metals and alloys in corrosive environments [J]. Acta Materialia, 2017, 130: 137−146.

[18] KRUEHONG C, EL-MAHDY G A, NISHIKATA A, TSURU T. Influence of second phases on the electrochemical behavior of hot dipped Al−Mg−Si coated steel [J]. Corrosion Science, 2010, 52(7): 2379−2386.

[19] YUAN Z P, TU Y Y, YUAN T, ZHANG Y H, HUANG Y H. Effect of post-brazing heat treatment on the corrosion mechanism of sandwich multi-layered aluminium sheets [J]. Vacuum, 2021, 183: 109781.

[20] YANG X J, YANG Y, SUN M H, JIA J H, CHENG X Q, PEI Z B, LI Q, XU D, XIAO K, LI X G. A new understanding of the effect of Cr on the corrosion resistance evolution of weathering steel based on big data technology [J]. Journal of Materials Science & Technology, 2022, 104: 67−80.

[21] ALVAREZ K L, AHMADIAN BAGHBADERANI H, MARTÍN J M, BURGOS N, MCCLOSKEY P, GONZÁLEZ J, MASOOD A. Novel predictive methodology of amorphisation of gas-atomised Fe−Si−B alloy powders [J]. Journal of Non-Crystalline Solids, 2021, 574: 121151.

[22] CHEN Y S, LU H Z, LIANG J T, ROSENTHAL A, LIU H W, SNEDDON G, MCCARROLL I, ZHAO Z Z, LI W, GUO A M, CAIRNEY J M. Observation of hydrogen trapping at dislocations, grain bound and precipitates [J]. Science, 2020, 367(6474): 171−175.

[23] CHEN Y S, HALEY D, GERSTL S S A, LONDON A J, SWEENEY F, WEPF R A, RAINFORTH W M, BAGOT P A J, MOODY M P. Direct observation of individual hydrogen atoms at trapping sites in a ferritic steel [J]. Science, 2017, 355(6330): 1196−1199.

[24] CHRISTODOULOU P, CALOS N. A step towards designing Fe−Cr−B−C cast alloys [J]. Materials Science and Engineering A, 2001, 301(2): 103−117.

[25] RÖTTGER A, LENTZ J, THEISEN W. Boron-alloyed Fe−Cr−C−B tool steels—Thermodynamic calculations and experimental validation [J]. Materials & Design, 2015, 88: 420−429.

[26] WANG Y, YANG L X, LIU R J, LIU H J, ZENG C L, ZHU S L, FU C. Ternary-layered Cr_2AlB_2 synthesized from Cr, Al, and B powders by a molten salt-assisted method [J]. Powder Technology, 2021, 387: 354−362.

[27] WANG W J, LIN J P, WANG Y L, CHEN G L. Isothermal corrosion Fe_3Si alloy in liquid zinc [J]. Journal of University of Science and Technology Beijing, 2007, 14(1): 52−55.

[28] WANG M M, XUE J, GAO R, GAO H Y, ZHOU Y, ZHAO Y Y, LIU Y H, KANG M D, WANG J. Interface morphology and corrosion behavior of bulk Fe_2B in liquid Al [J]. Materials Characterization, 2019, 152: 1−11.

[29] YIN F C, ZHAO M X, LIU Y X, HAN W, LI Z. Effect of Si on growth kinetics of intermetallic compounds during reaction between solid iron and molten aluminum [J]. Transactions of Nonferrous Metals Society of China, 2013, 23(2): 556−561.

[30] de GRAEVE I, SCHOUKENS I, LANZUTTI A, ANDREATTA F, ALVAREZ-PAMPLIEGA A, de STRYCKER J, FEDRIZZI L, TERRYN H. Mechanism of corrosion protection of hot-dip aluminium-silicon coatings on steel studied by electrochemical depth profiling [J]. Corrosion Science, 2013, 76: 325−336.

[31] COUTO C P, ANDREATTA F, LANZUTTI A, COSTA I, PANOSSIAN Z, DE GRAEVE I, TERRYN H, ROSSI J L, REVILLA R I. Depth profiling approach to evaluate the influence of hot stamping on the local electrochemical

behaviour and galvanic series of hot-dip Al−Si coating on 22MnB5 steel[J]. Corrosion Science, 2021, 185: 109435.
[32] PRADHAN D, MANNA M, DUTTA M. Al−Mg−Mn alloy coating on steel with superior corrosion behavior [J]. Surface and Coatings Technology, 2014, 258: 405−414.
[33] LIU H X, HUANG F, YUAN W, HU Q, LIU J, CHENG Y F. Essential role of element Si in corrosion resistance of a bridge steel in chloride atmosphere [J]. Corrosion Science, 2020, 173: 108758.
[34] KUMAR S, MAJUMDAR S, PAUL B, KISHOR J, KAIN V. Kinetics of formation of pack aluminized coating on 9Cr−1Mo steel and interdiffusional behaviour of iron aluminides at intermediate temperatures [J]. Surface and Coatings Technology, 2021, 426: 127794.
[35] LI L, GUO P, LIU L L, LI X W, KE P L, WANG A Y. Structural design of Cr/GLC films for high tribological performance in artificial seawater: Cr/GLC ratio and multilayer structure [J]. Journal of Materials Science & Technology, 2018, 34(8): 1273−1280.
[36] NEMATI N, BOZORG M, PENKOV O V, SHIN D G, SADIGHZADEH A, KIM D E. Functional multi-nanolayer coatings of amorphous carbon/tungsten carbide with exceptional mechanical durability and corrosion resistance [J]. ACS Applied Materials & Interfaces, 2017, 9(35): 30149−30160.
[37] BAHADORMANESH B, GHORBANI M. Ni-P/Zn-Ni compositionally modulated multilayer coatings. Part 2: Corrosion and protection mechanisms [J]. Applied Surface Science, 2018, 442: 313−321.
[38] CUBIDES Y, KARAYAN A I, ZHAO D X, NASH L, XIE K, CASTANEDA H. New insights on the corrosion mechanism of a peak-aged Mg−9Al−1Zn alloy in a chloride environment [J]. Journal of Alloys and Compounds, 2020, 840: 155786.
[39] WANG Z Y, MA G S, LI Z C, RUAN H T, YUAN J H, WANG L, KE P L, WANG A Y. Corrosion mechanism of Ti_2AlC MAX phase coatings under the synergistic effects of water vapor and solid NaCl at 600 ℃ [J]. Corrosion Science, 2021, 192: 109788.

热扩散处理对热浸镀铝 Fe−Cr−Si−B 铸钢组织演变及腐蚀行为的影响

张先满[1]，陈再雨[1]，李星涛[1]，季坤鹏[1]，罗洪峰[1]，万耿平[2]，杨少锋[3]

1. 海南大学 机电工程学院，海口 570228；
2. 海南大学 分析测试中心，海口 570228；
3. 南京理工大学 材料科学与工程学院，南京 211167

摘 要：研究热扩散处理对热浸镀铝 Fe−Cr−Si−B 铸钢镀层组织及在 5% (质量分数) NaCl 溶液中的腐蚀行为的影响。结果表明：Fe−Cr−Si−B 铸钢中的 Fe 基体与 Al 液界面反应产物为柱状结构的 $FeAl_3$。在$(Cr,Fe)_2B$/Al 界面上形成的周期性层片结构是在热扩散处理过程中形成，而非热浸镀铝。在短时间内表面残留 Al 层主导了热浸镀铝和热扩散处理镀层在 NaCl 溶液中的腐蚀行为，直到表面残留 Al 层被完全消耗。Cl^-引起的点蚀优先从块状 B−Al−Cr 相与 $FeAl_3$ 的界面开始，并沿周期性层片结构扩展。硅颗粒作为阴极，促进了镀层的腐蚀。在 Fe−Al 金属间化合物层被完全腐蚀之前，钢基体都处于阴极保护中。此外，高温 NaCl 溶液的腐蚀被显著加速。

关键词：热浸镀铝；热扩散处理；周期性层片结构；腐蚀行为；阴极保护

(Edited by Xiang-qun LI)